Predictive capabilities of data-driven machine learning techniques on wave-bridge interactions

Deming Zhu, Jiaxin Zhang, Qian Wu, You Dong, Emilio Bastidas-Arteaga

Please cite this preprint as: Zhu, D., Zhang, J., Wu, Q., Dong, Y., and Bastidas-Arteaga E. (2023) Predictive capabilities of data-driven machine learning techniques on wave-bridge interactions. Applied Ocean Research, 137, 103597. doi: https://doi.org/10.1016/j.apor.2023.103597

Predictive capabilities of data-driven machine learning techniques on wave-bridge interactions

Deming Zhu[1], Jiaxin Zhang[1], Qian Wu[1,2], You Dong[1,3]*, Emilio Bastidas-Arteaga[4]

To explore coastal bridge safety subjected to extreme waves during coastal natural hazards, numerical simulations that combine finite element methods and experimental data have been recognized as effective in computing wave-induced loads on coastal bridges. However, the structural design and performance assessment for bridge networks require laborious efforts and massive computational resources to account for uncertain scenarios. To provide reliable wave force estimation tools and facilitate the associated risk assessment, this study performs a hydrodynamic experiment on the wave-bridge interactions and develops data-driven Long-Short-Term-Memory (LSTM) Machine Learning (ML) models for time series forecasting of wave forces. Specifically, a 1:30 scale bridge superstructure specimen is used for the wave test in the wave channel. Different solitary wave and regular wave conditions are tested. Time histories of wave profiles, wave-induced forces, and pressures are measured and served as a dataset basis for the training of LSTM models. High-performance LSTM prediction models are developed through the tuning of different hyperparameters. The well-trained models have high accuracy and could predict the wave force time series based on the excitation wave profiles in seconds. It is envisioned that LSTM models could provide more reliable estimations with the development based on more data sources, providing a fast path for structural design, analysis, and maintenance.

Keywords: Coastal bridge; Hydrodynamic experiment; Wave force prediction; LSTM; Machine learning

[1] Department of Civil and Environmental Engineering, The Hong Kong Polytechnic University, Hong Kong, China.
[2] Department of Ocean Science and Engineering, Southern University of Science and Technology, Shenzhen, China.
[3] Research Institute for Sustainable Urban Development, The Hong Kong Polytechnic University, Hong Kong, China
[4] Department of Civil Engineering, La Rochelle University, France
* Corresponding Author: you.dong@polyu.edu.hk.

1. Introduction

As an essential component of transportation systems in nearshore cities, the safety of coastal bridges is often threatened by the hostile natural environment. Due to the increasing hazard intensity and sea level rise caused by global climate change, tropical cyclone and tsunami-induced waves have resulted in severe damage to low-lying bridges in recent decades. According to the post-hazard survey, Hurricane Ivan in 2004 was responsible for 58 bridge span damages being unseated from the piers and 66 spans being misaligned (Meng and Jin 2007). In the next year, Hurricane Katrina caused severe damage to coastal bridges once again, including the US 90 highway bridge over Biloxi Bay, the US 90 highway bridge over Bay St. Louis, and a box-girder railroad bridge (Robertson et al. 2011). The deck unseating failure, which refers to the unexpected bridge span fall under extreme wave impacts, has been recognized as one of the critical failure modes of coastal bridges (Ataei and Padgett 2013; Azadbakht and Yim 2016; Robertson et al. 2007). This has motivated a number of studies to assess the magnitudes of wave loads and bridge damage mechanisms in past years.

To date, a series of physical tests have been carried out to study the huge wave forces acting on bridge spans (Guo et al. 2016; Istrati and Buckle 2019; Qu et al. 2018; Seiffert et al. 2014; Seiffert et al. 2015; Zhang et al. 2020), but an accurate estimation method has not been promoted. Motivated by the extensive coastal bridge damages during Hurricane Ivan in 2004 and Hurricane Katrina in 2005, Douglass et al. (2006) conducted a large-scale test to investigate periodic wave-induced forces on a bridge span and proposed some basic empirical formulas to estimate the maximum vertical and horizontal wave forces. Bradner et al. (2011) measured the wave loads on a 1:5 scale reinforced concrete model of the I-10 type bridge span and investigated the effects of different wave parameters. Cuomo et al. (2009) reported their experimental studies on a 1:10 scale bridge model and pointed out the adverse effects due to the trapped air beneath the deck. Although the first guideline for estimating wave forces acting on the coastal bridges was then published based on the physics-based method (AASHTO 2008), several key factors are still not clear due to the lack of data support. For instance, Guo et al. (2016) compared their experimental measured loads with the wave forces estimated using

empirical formulas. They found that the AASHTO method tends to underestimate the vertical force at a smaller wave height but significantly overpredict the vertical force when the specimen is fully submerged. A similar phenomenon was observed in the simulations of focused wave groups conducted by Moideen and Behera (2021), that the AASHTO formulae highly underestimate the peak vertical impact force for lower wave heights and moderately capture the peak vertical impact force at higher wave heights. Besides, the applicability of AASHTO formulas is also limited to their focused wave conditions, while accurate predictions are not available for other scenarios. To overcome these shortages, a few more experimental studies were then carried out in recent years (Xiang and Istrati 2021; Zhu et al. 2022; Zhu and Dong 2020). Nevertheless, an accurate wave force estimation method has not been reached, and more relevant studies are required to develop existing formulas. To fulfill the research gap on this point, this study carries out an experimental study to investigate wave-bridge interactions. Two different wave shapes, regular waves and solitary waves are tested to explore the extreme waves caused by tropical cyclones and tsunamis, respectively.

Another significant problem associated with the study of wave-bridge interactions lies in the shortage of time series analysis. Although several experimental tests and numerical simulations have been conducted to measure the wave loads, most of them mainly focused on the maximums of vertical and horizontal forces but neglected the changing process of pressure distributions (Jin and Meng 2011; Seiffert 2014; Seiffert et al. 2016). One direct consequence is that the subsequent performance assessments mostly rely on static structural analysis, which typically compared the maximum load with the static bridge capacity. Such a method cannot fully predict the potential risks induced by periodic wave impacts during a real storm hazard and may mislead the maintenance and management strategies for high-risk bridges (Zhu et al. 2021). Dynamic analysis of wave-bridge interactions has aroused growing concern in recent years. For example, Xu et al. (2018) performed time-domain simulations to compute the combined effects of wind and waves on a three-span suspension bridge and found it challenging to determine appropriate intensity measures to be considered in the structural design. Yuan et al. (2021) investigated the performance of bearing connections under dynamic wave impacts

and found that the structural responses are highly dependent on the connection stiffness. Ding et al. (2018) investigated the combined earthquake and wave-current effects on bridge piers and highlighted the enlarged responses caused by the long-period hazards. All of these studies pointed out the necessity of an insight understanding of the time history effects of wave impacts. To address this issue, time histories of vertical and horizontal wave forces, as well as the hydraulics pressures beneath the deck under various wave scenarios are measured. These results not only intuitively reflect the effects of different wave parameters, but also provide datasets for the training of prediction models in the following sections.

Experiments are reliable approaches for acquiring wave forces on coastal bridges but could be extremely expensive and difficult for large-scale investigations (Xu et al. 2022). Scientists and engineers tried to establish full-scale numerical models to compute approximations for various hazard scenarios, while it is often prohibitive to form a sufficiently large database for its unbearable computational cost, especially for the reliability and life-cycle analysis involving large-scale computations (Chorzepa et al. 2016; Dong and Frangopol 2016; Jia et al. 2022; Xiao and Huang 2008). To overcome this limitation, machine learning (ML) methods have been utilized to establish the relationship between input hazard intensities and output structural responses. For example, Xu et al. (2022) examined the prediction performance of different ML technologies. It was found that ML models have superior abilities to estimate the maximum wave forces, but more datasets are required to improve the model quality. Besides, to facilitate the risk assessment and proposition of mitigation measures, Zhu et al. (2021) utilized ML models to replace the time-consuming simulations and achieved satisfying results. However, a similar problem is that existing ML technologies typically focus on the peak values, but investigations on the time series effects are limited. Xu et al. (2023) performed a state-of-the-art review on ML technologies in coastal bridge hydrodynamics and observed that the time series predictions involving sequential data are relatively less. Also, numerical simulation is still the main source of training data. To address this issue, this study develops a Long Short-Term Memory (LSTM) network based on the wave force time histories measured in the experiment. Different hyperparameters are tuned and validated to improve the model's

accuracy. The optimization model demonstrates good performance in forecasting wave forces under different wave scenarios.

Overall, this study aims to investigate the wave impacts on coastal bridge superstructures and develop data-driven ML techniques for the prediction of time series results. Time histories of wave forces and pressures are investigated through laboratory experiments. LSTM models are established to forecast wave impacts based on the measured wave profiles. The proposed data-driven LSTMs can be an alternative to relieve the laboriousness and high cost of experimental and numerical simulations on the wave-bridge interactions. The rest parts of this paper are organized as follows. Section 2 introduces the laboratory testing of wave-bridge interactions, including experimental design, laboratory facilities, and wave models. Section 3 gives an overview of the LSTM method utilized in this study. Section 4 presents the measured wave forces and pressures under different wave conditions. Section 5 shows the fitting results using the LSTM method and discusses the prediction performance of the promoted method. Finally, conclusions, limitations, and future works are given in Section 6.

2. Laboratory testing of wave-bridge interactions

Laboratory tests are conducted in conjunction with activities at the Hydraulics Laboratory of the Hong Kong Polytechnic University. A bridge deck mock-up is tested at the wave channel to evaluate the structural performance during wave impacts. Measured datasets are mainly used for two purposes: (a) quantifying adverse impacts induced by waves and comparisons with existing methods and (b) providing a database for the machine learning models.

2.1 Investigated bridge and extreme wave model

The investigated bridge is one span of a simply supported bridge as shown in Fig. 1(a). This type of US-90 bridge played an important role in transportation networks over Biloxi Bay, Mississippi, but was severely destroyed in a category-5 storm Hurricane Katrina in 2005 (Robertson et al. 2007). These segments vary from 13.7 m to 15.9 m. Each segment consists of six prestressed concrete girders and three pairs of diaphragms are settled between each girder. However, the bearing connections between the deck and the bent are not strong enough to resist

extreme wave impacts. The air could be trapped between the girders and increase the uplift loads, which means these segments were nearly buoyant once submerged (Robertson et al. 2006). Also, similar superstructure designs have been utilized in many other coastal highway bridges, so this type of bridge is adopted as a representative example in this study. As shown in Fig. 1(b), the selected bridge span has a length of 15.85 m and a width of 10.8 m. The girder height is 1.37m and the deck thickness is 0.18 m. The overlength out of the two sides of the deck is taken as 0.5 m.

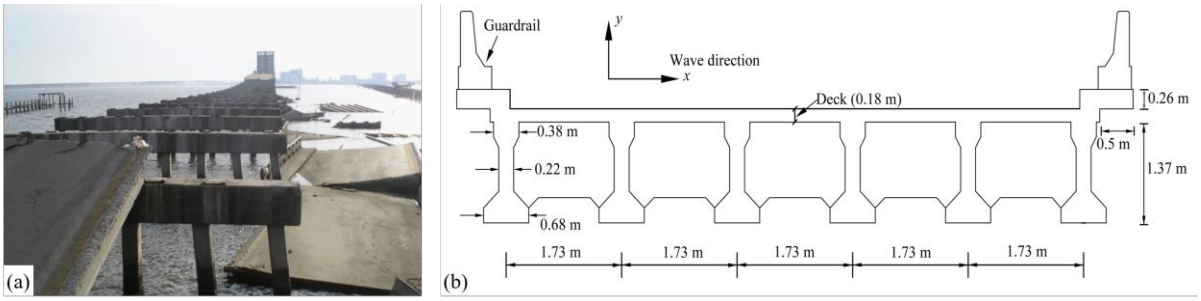

Fig. 1 (a) Span unseating failure of US-90 Biloxi-Ocean Springs Bridges during Hurricane Katrina (Padgett et al. 2008) and (b) dimensions of the investigated bridge span

2.2 Experimental facilities and tested cases

A 1:30 scale experiment is designed according to the open channel Froude similarity law and conducted at the wave channel at the hydraulics laboratory. The Froude scale model is suitable for phenomena where gravity and inertial forces are dominant, particularly for free surface flows (e.g., coastal structures and waves). A schematic diagram of the wave channel and photos of different facilities are shown in Fig. 2(a). Surface waves are generated in the wave channel, which has a total length of 27 m, a width of 1.5 m, and a depth of 1.5 m. The span model is made of an acrylic board (as shown in Fig. 2(c)) and fixed to a platform in the middle section of the channel using steel bars. The distance from the girder bottom to the channel is 0.55 m. After being converted to the 1:30 laboratory scale, the plastic-made mock-up size is about 0.53 m in length and 0.36 m in width, as shown in Fig. 2(b). Wave forces on the span are measured using a multi-axis wave load. Multiple pressure gauges are settled (as shown in Fig. 2(b)) to record the changing pressure caused by the water surface elevation and trapped air beneath the deck.

Two types of waves, regular waves and solitary waves are tested to account for the extreme waves induced by tropical cyclones and tsunamis, respectively. The storm-induced waves are highly periodic in nature, while tsunami waves are often caused by the displacement of a significant volume of water under the sea. A total of 98 regular wave cases and 30 solitary wave cases are tested, as listed in Table 1 and Table 2, respectively. Each case is repeatedly tested 5 times to avoid experimental monitoring deviations. The surface wave functions of these two types of waves are given as

$$\eta_{\text{solitary}}(x,t) = H \operatorname{sech}^2 \sqrt{\frac{3}{4}\frac{H}{D^3}}(x-ct) \tag{1}$$

$$\eta_{\text{regular}}(x,t) = A\cos\left[k(x-ct)\right] \tag{2}$$

where η = water surface elevation; H = wave height; D = water depth; c = wave celerity; A = amplitude; k = wave number; x = coordinate; and t = time. Detailed introduction of experimental facilities, control strategies, and stability validations of the generated waves can be found in the authors' previous work (Zhu et al. 2022; Zhu and Dong 2020).

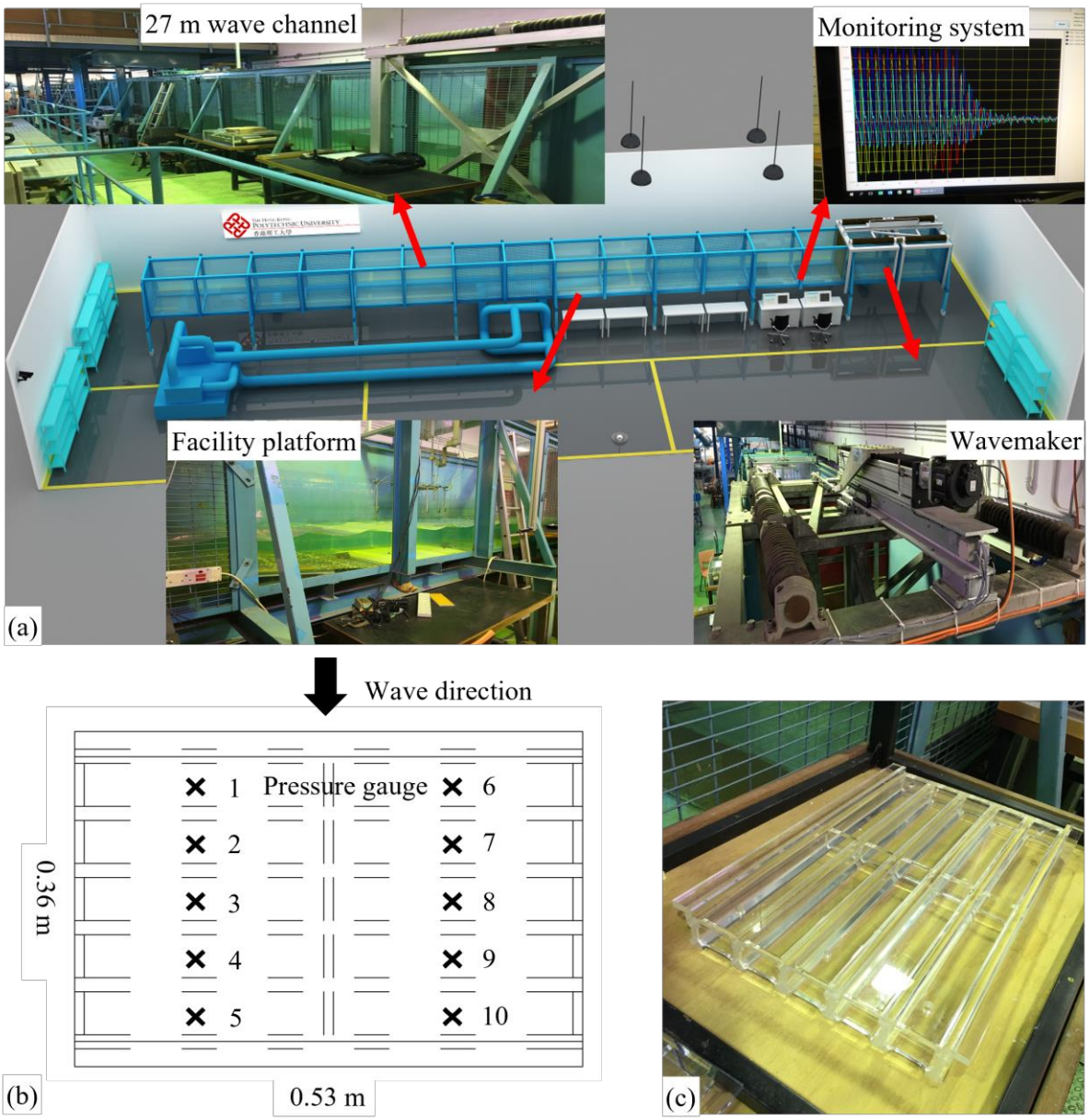

Fig. 2 (a) Schematic diagram of the hydraulics laboratory and photos of experimental facilities; (b) dimensions of the span model (top view) and distributions of the pressure gauges; and (c) photo of the acrylic board span model

Table 1 Tested regular wave cases

No.	*D* (m)	*H* (m)	*T* (s)	No.	*D* (m)	*H* (m)	*T* (s)	No.	*D* (m)	*H* (m)	*T* (s)
1	0.48	0.14	1	34	0.52	0.12	1.2	67	0.54	0.12	1.8
2	0.48	0.14	1.2	35	0.52	0.12	1.4	68	0.54	0.12	2
3	0.48	0.14	1.4	36	0.52	0.12	1.6	69	0.54	0.14	1
4	0.48	0.14	1.6	37	0.52	0.12	1.8	70	0.54	0.14	1.2
5	0.48	0.16	1	38	0.52	0.12	2	71	0.54	0.14	1.4

6	0.48	0.16	1.2	39	0.52	0.14	1	72	0.54	0.14	1.6
7	0.48	0.16	1.4	40	0.52	0.14	1.2	73	0.54	0.14	1.8
8	0.48	0.16	1.6	41	0.52	0.14	1.4	74	0.54	0.14	2
9	0.50	0.12	1	42	0.52	0.14	1.6	75	0.56	0.08	1
10	0.50	0.12	1.2	43	0.52	0.14	1.8	76	0.56	0.08	1.2
11	0.50	0.12	1.4	44	0.52	0.14	2	77	0.56	0.08	1.4
12	0.50	0.12	1.6	45	0.52	0.16	1	78	0.56	0.08	1.6
13	0.50	0.12	1.8	46	0.52	0.16	1.2	79	0.56	0.08	1.8
14	0.50	0.12	2	47	0.52	0.16	1.4	80	0.56	0.08	2
15	0.50	0.14	1	48	0.52	0.16	1.6	81	0.56	0.1	1
16	0.50	0.14	1.2	49	0.52	0.16	1.8	82	0.56	0.1	1.2
17	0.50	0.14	1.4	50	0.52	0.16	2	83	0.56	0.1	1.4
18	0.50	0.14	1.6	51	0.54	0.08	1	84	0.56	0.1	1.6
19	0.50	0.14	1.8	52	0.54	0.08	1.2	85	0.56	0.1	1.8
20	0.50	0.14	2	53	0.54	0.08	1.4	86	0.56	0.1	2
21	0.50	0.16	1	54	0.54	0.08	1.6	87	0.56	0.12	1
22	0.50	0.16	1.2	55	0.54	0.08	1.8	88	0.56	0.12	1.2
23	0.50	0.16	1.4	56	0.54	0.08	2	89	0.56	0.12	1.4
24	0.50	0.16	1.6	57	0.54	0.1	1	90	0.56	0.12	1.6
25	0.50	0.16	1.8	58	0.54	0.1	1.2	91	0.56	0.12	1.8
26	0.50	0.16	2	59	0.54	0.1	1.4	92	0.56	0.12	2
27	0.52	0.10	1	60	0.54	0.1	1.6	93	0.56	0.14	1
28	0.52	0.10	1.2	61	0.54	0.1	1.8	94	0.56	0.14	1.2
29	0.52	0.10	1.4	62	0.54	0.1	2	95	0.56	0.14	1.4
30	0.52	0.10	1.6	63	0.54	0.12	1	96	0.56	0.14	1.6
31	0.52	0.10	1.8	64	0.54	0.12	1.2	97	0.56	0.14	1.8
32	0.52	0.10	2	65	0.54	0.12	1.4	98	0.56	0.14	2
33	0.52	0.12	1	66	0.54	0.12	1.6				

Table 2 Tested solitary wave cases

No.	D (m)	H (m)	No.	D (m)	H (m)	No.	D (m)	H (m)	No.	D (m)	H (m)
1	0.48	0.1	9	0.5	0.14	17	0.52	0.18	25	0.56	0.1
2	0.48	0.12	10	0.5	0.16	18	0.52	0.2	26	0.56	0.12
3	0.48	0.14	11	0.5	0.18	19	0.54	0.1	27	0.56	0.14
4	0.48	0.16	12	0.5	0.2	20	0.54	0.12	28	0.56	0.16
5	0.48	0.18	13	0.52	0.1	21	0.54	0.14	29	0.56	0.18
6	0.48	0.2	14	0.52	0.12	22	0.54	0.16	30	0.56	0.2
7	0.5	0.1	15	0.52	0.14	23	0.54	0.18			
8	0.5	0.12	16	0.52	0.16	24	0.54	0.2			

3. Overview of LSTM methodology

For a considerable length of time, one of the primary difficulties that plagued conventional neural network architectures was the incapacity to interpret input sequences that were dependent on each other for relevant information (Sherstinsky 2020; Zhang et al. 2021). Traditional neural networks receive an independent data vector on each occasion and lack the ability to store information in memory to assist with memory-dependent tasks. To address this limitation, a novel class of Recurrent Neural Networks (RNNs) was developed. This approach utilizes a straightforward feedback mechanism for neurons in the network, whereby the output is returned to the input to provide information about the most recent inputs. Another issue associated with RNNs is the vanishing gradient problem. The vanishing gradient problem is essentially a situation in which an RNN cannot propagate useful gradient information from the output end of the model back to the layers near the input end of the model. It may result in models with many layers being rendered unable to learn on a specific dataset. and could even cause models with many layers to prematurely converge to a substandard solution (Hochreiter 1998).

To counteract the aforementioned drawback of RNN, an LSTM network is built to predict wave force time series from the measured wave profiles. In accordance with the Universal Approximation Theorem posited by Robert Hecht-Nielsen (Hecht-Nielsen 1992), an LSTM neural network endowed with a hidden layer is capable of effectuating a mapping between finite-dimensional spaces. This holds true as long as the network boasts an adequate assemblage of hidden neurons, and the greater the number of said neurons, the more heightened veracity of the network's approximation. Within the confines of the present paper, an LSTM neural network equipped with hidden layers is appropriated as a prediction model for time series wave loads. The LSTM model is built on the RNN architecture by incorporating four states into a single recurrent structure. These states facilitate the persistence of a unit that determines the retention of input information. Each layer of the LSTM is comprised of one recurrent structure. The frequency of self-updates in the overall structure is dictated by the dimensions of the input data and the number of cycles, so the current LSTM layer only requires the computation of one recurrent unit, instead of multiple consecutive units.

The network structure of a typical LSTM cell is shown in Fig. 3, where X = input state to the cell; Y = output state of the cell; t = the number of the cell; h = hidden state output; c = cell state memory; σ = logistic sigmoid function; and tanh = hyperbolic tangent function. The LSTM cell works as follows: the input gate controls the amount of input data from the current network that is stored in the unit at the present time; the forget gate assesses the extent of the state transition from the previous time to the present time; and the output gate governs the output of the current unit state.

Two performance indicators, mean squared error (MSE) and the R^2-score, are used to evaluate the prediction performance of the established LSTM models. MSE is the metric typically used as a loss function to be minimized during network training. The main limitation of the MSE is that the assumed numerical values are not normalized with respect to the variability of the data. To overcome this point, the R^2-score can measure the predictive power of a given model with respect to the predictive power of the trivial model, which always forecasts the mean value of the observed data (i.e., $R^2 = 0$). The R^2-score is widely used because it can be seen as a normalized version of the R^2. These two indicators are calculated as

$$MSE(y,\hat{y}) = \frac{1}{N}\sum (y-\hat{y})^2 \tag{3}$$

$$R^2(y,\hat{y}) = 1 - \frac{MSE(y,\hat{y})}{MSE(y,\bar{y})} = 1 - \frac{\sum (y-\hat{y})^2}{\sum (y-\bar{y})^2} \tag{4}$$

where y = the measured data in the experiment; y' = the predicted value using LSTMs; and $\bar{y}$ = mean of the truth data.

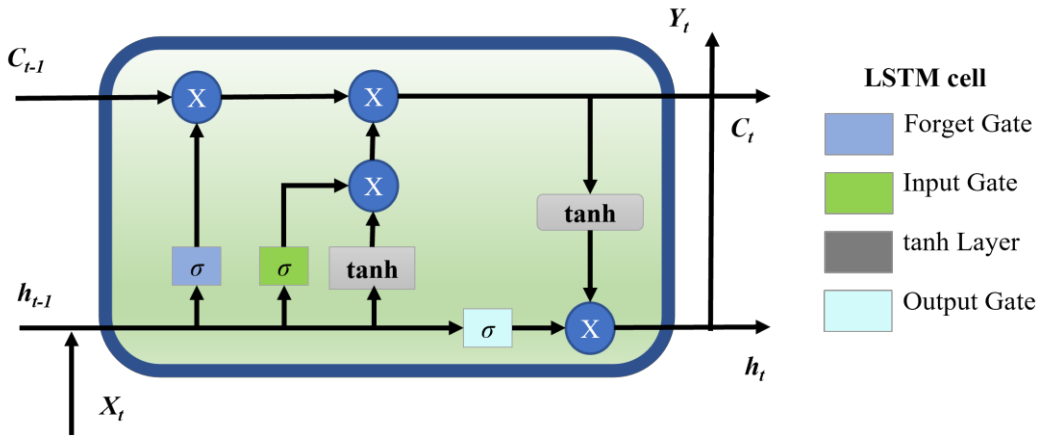

Fig. 3 Network structure of a typical LSTM cell

4. Wave-induced forces and comparisons with previous studies

The wave loads on the bridge span are dependent on both structural dimensions and wave parameters, so impacts caused by regular waves and solitary waves are investigated separately. To obtain more insight into wave force characteristics, vertical and horizontal wave forces as well as the hydraulics pressure on the specimen are analyzed.

4.1 Solitary wave results

By collecting the measured results from the load cell and pressure gauges, Fig. 4 shows three typical time series results of vertical forces and pressures applied on the specimen under solitary wave cases with D = 0.48 m and H = 0.18 m, D = 0.52 m and H = 0.18 m, and D = 0.56 m and H = 0.18 m. Because of the symmetric distributions of the pressure gauges, only the measured data from gauges 1-5 are presented. As shown in Fig. 4, both the wave forces and pressures increase to a maximum value and then drop to a valley as the propagation of solitary waves. For a constant wave height H = 0.18 m, the maximum values of vertical forces F_y increase from 74.15 to 113.64 N as water depth increases. However, there are little changes in the maximums of horizontal forces F_x, which are around 47.90 N, 40.17 N, and 43.80 N respectively. For the wave pressures, pressures measured at the seaward side facing the waves, i.e., wave gauge 1, are around 20-30% larger than those measured at the opposite side. This means that not only the concrete components in these areas are subject to greater impacts, but also the connections may suffer from higher loads. In addition, the pressures decrease to a

254 negative value after the wave crest passes the span, and the downward forces are caused by the
255 vacuum area created beneath the span when the water surface drops rapidly. The minimum
256 negative pressures reduce for larger water depths and are around -266.74 Pa, -334.49 Pa, and -
257 342.26 Pa, respectively. Most of the previous studies only focuses on the maximum vertical
258 and horizontal forces induced by extreme waves, but recent ones have pointed out the
259 concentrated wave pressure and the subsequent overturning moment could also be critical
260 reasons for span failure (Cai et al. 2018; Istrati and Buckle 2019; Zhu et al. 2021). Therefore,
261 both the maximum wave forces and pressures are analyzed in the following sections.

262 By tracing the time histories of the monitored data, the maximum values of vertical force,
263 horizontal force, and pressure are collected and presented in Fig. 5. The final results are taken
264 by removing the maximum and minimum values from all five trials for each wave case, and
265 then averaging the rest results. The projections of the maximums on the *xz*-plane are plotted as
266 well. It should be noted that all of the pressure results are taken from pressure gauge 1 since it
267 records the highest pressure for all the cases. From the test results, the following can be
268 observed: (a) The maximums of F_y, and P show a close-linear relationship with both wave
269 height H and water depth D. However, F_x only increases for larger H, but changes little with D.
270 (b) The maximum pressure for the tested cases is 1362.58 Pa, which equals 40.88 kPa after
271 being converted to a prototype scale. The concentrated pressure at the seaward side is around
272 20-30% over the average value. (c) Solitary wave-induced impacts are mainly affected by the
273 wave height H and the water depth (or clearance between the water level and the bridge span).
274 This phenomenon is consistent with its characteristics, that the solitary waves are non-periodic
275 fluctuations with their volume and energy highly concentrated.

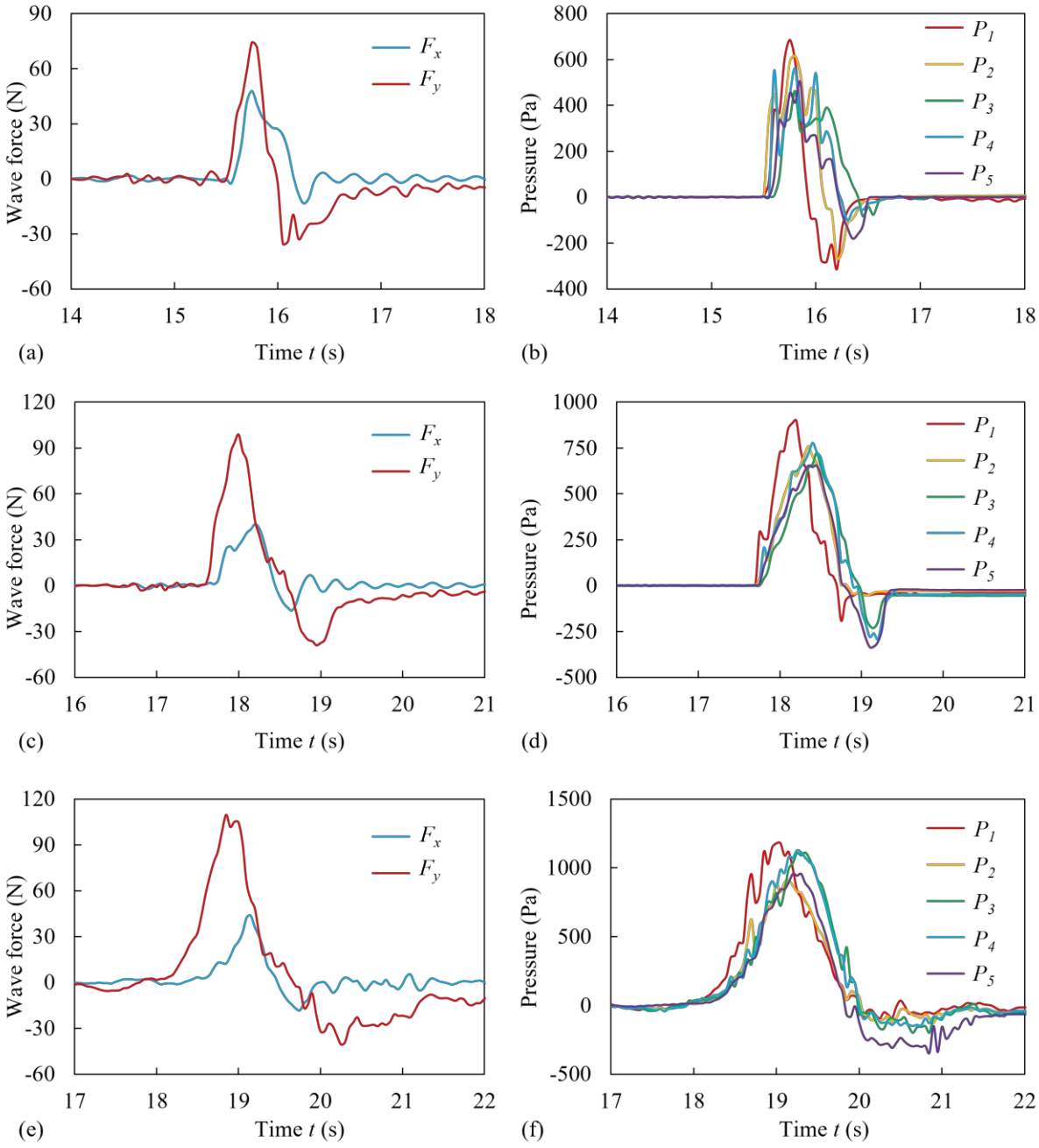

Fig. 4 Time histories of (a) wave force for case D = 0.48 m and H = 0.18 m; (b) surface pressure for case D = 0.48 m and H = 0.18 m; (c) wave force for case D = 0.52 m and H = 0.18 m; (d) surface pressure for case D = 0.52 m and H = 0.18 m; (e) wave force for case D = 0.56 m and H = 0.18 m; and (f) surface pressure for case D = 0.56 m and H = 0.18 m

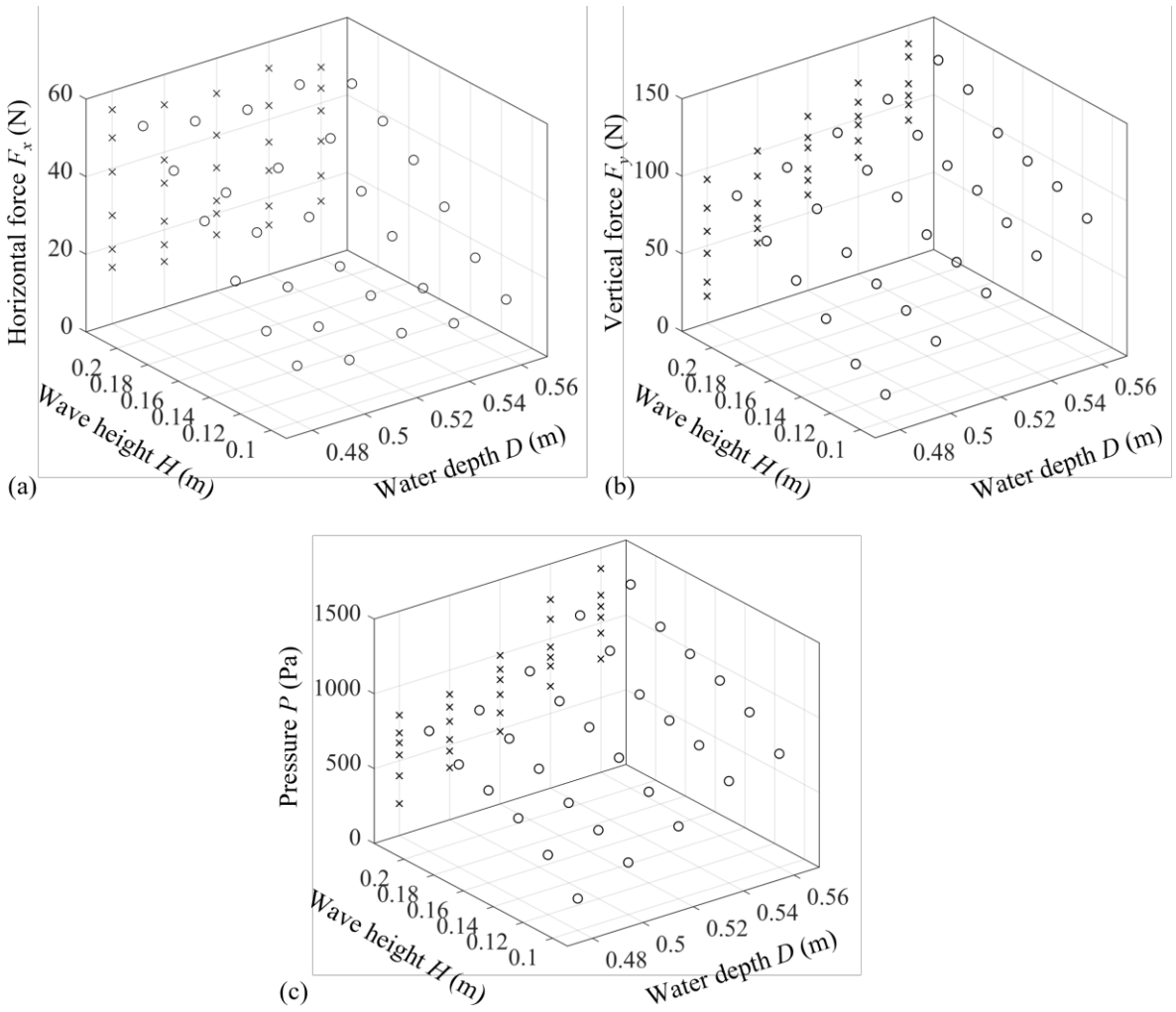

Fig. 5 Maximums of solitary wave impacts: (a) maximum horizontal force; (b) maximum vertical force; and (c) maximum pressure

4.2 Regular wave results

Time series results of representative cases are plotted in Figs 6 and 7. Different from solitary waves, although the load and pressure also experience periodic positive and negative changes as the water surface rises and falls, they are dependent on the wave period T as well. Fig. 6 compares the effects of different periods (T = 1.2 s, 1.4 s, and 2.0 s) under a constant water depth (D = 0.52 m) and wave height (H = 0.14 m). The peak values of F_y decrease from 71.70 to 27,97 N as wave period T increases. For the horizontal force F_x and pressure P, the maximums also decrease from 43.31 to 12.86 N and from 1808.20 to 466.53 Pa, respectively. As shown in Fig. 7 for the cases with D = 0.56 m and H = 0.14 m, another difference between solitary and regular waves lies in the maximum pressure. Pressure gauge 1 always measures

295 the largest P among all the solitary wave conditions, while it may occur at different positions
296 under regular wave conditions, e.g., P_5 = 1858.12 Pa and P_3 = 760.32 Pa.

297 Maximum horizontal force, vertical force, and pressure under different wave conditions
298 are plotted in Figs. 8-10. As indicated, F_x, F_y, and P all increase for larger wave height H.
299 However, the maximum values are observed when water depth D = 0.52 and 0.54 m (i.e.,
300 clearances between the girder bottom and initial water surface equal 0.03 and 0.01 m), which
301 is F_x = 54.35 N, F_y = 93.83 N, and P = 2304.54 Pa, respectively. For the effects of wave period
302 T, the wave impacts show a trend of first increasing and then decreasing as the T grows. The
303 peak values are always observed when T is around 1.2 – 1.4 s, i.e., corresponding wavelength
304 λ ranges from 2.03 – 2.66 m, frequency v ranges from 4.49 – 6.28 Hz, and the non-dimensional
305 parameter deck-wavelength ratio from 0.14 – 0.24. This phenomenon indicates that, in the
306 design stage of coastal bridges, the structural dimensions of the span can be adjusted to mitigate
307 the wave impacts.

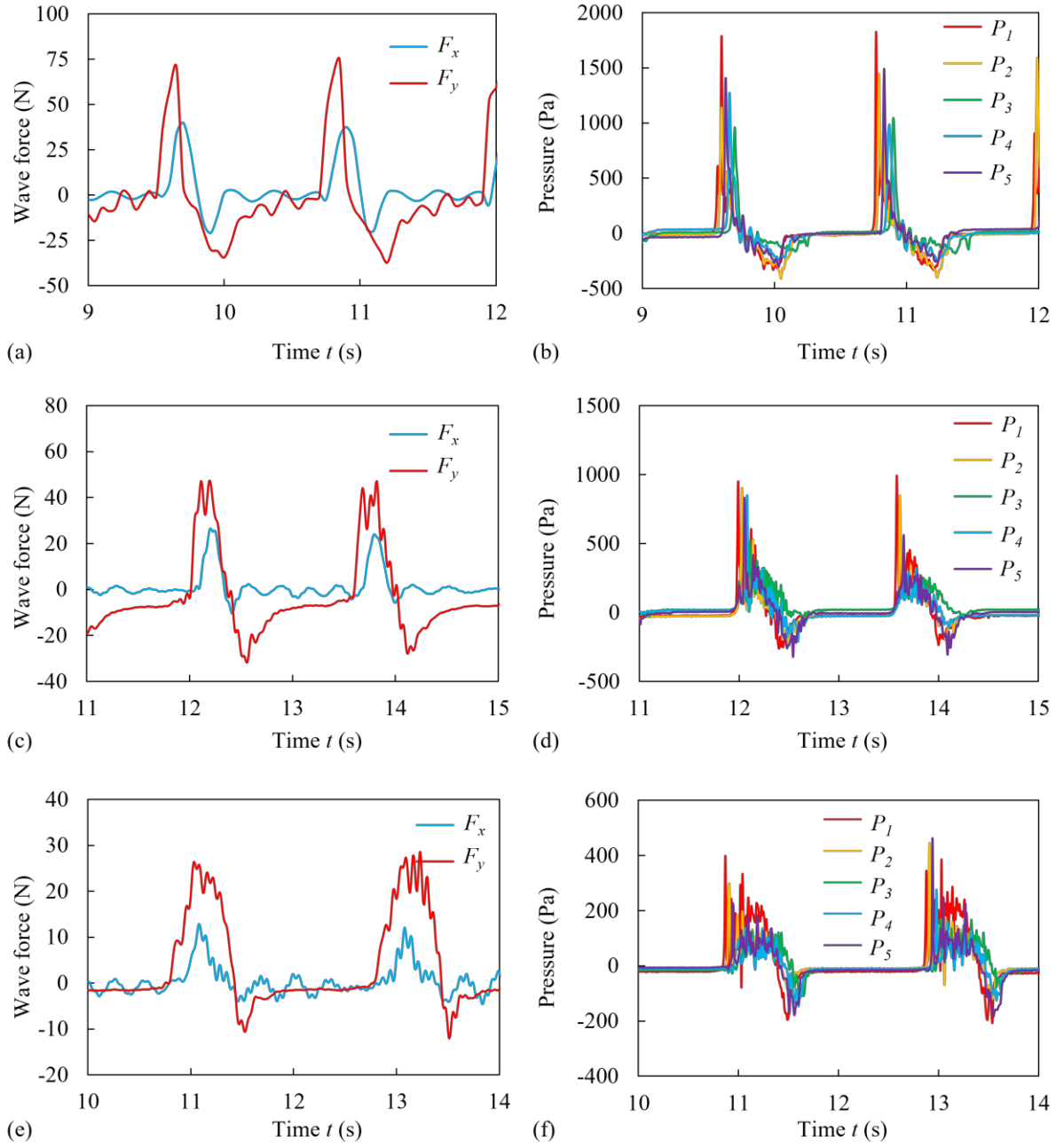

Fig. 6 Time histories of (a) wave force for case D = 0.52 m, H = 0.14 m, and T = 1.2 s; (b) surface pressure for case D = 0.52 m, H = 0.14 m, and T = 1.2 s; (c) wave force for case D = 0.52 m, H = 0.14 m, and T = 1.6 s; (d) surface pressure for case D = 0.52 m, H = 0.14 m, and T = 1.6 s; (e) wave force for case D = 0.52 m, H = 0.14 m, and T = 2.0 s; and (f) surface pressure for case D = 0.52 m, H = 0.14 m, and T = 2.0 s

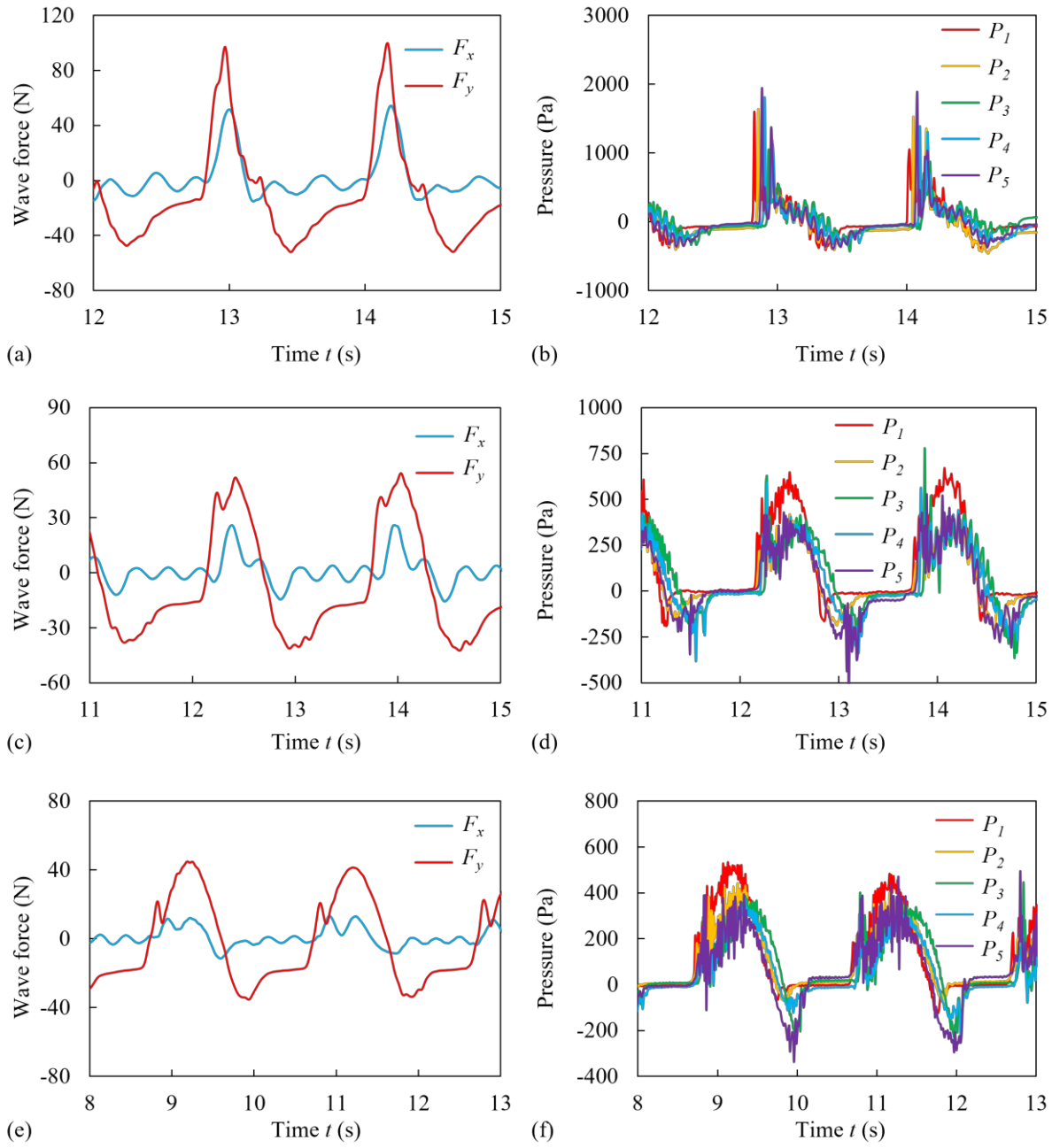

Fig. 7 Time histories of (a) wave force for case D = 0.56 m, H = 0.14 m, and T = 1.2 s; (b) surface pressure for case D = 0.56 m, H = 0.14 m, and T = 1.2 s; (c) wave force for case D = 0.56 m, H = 0.14 m, and T = 1.6 s; (d) surface pressure for case D = 0.56 m, H = 0.14 m, and T = 1.6 s; (e) wave force for case D = 0.56 m, H = 0.14 m, and T = 2.0 s; and (f) surface pressure for case D = 0.56 m, H = 0.14 m, and T = 2.0 s

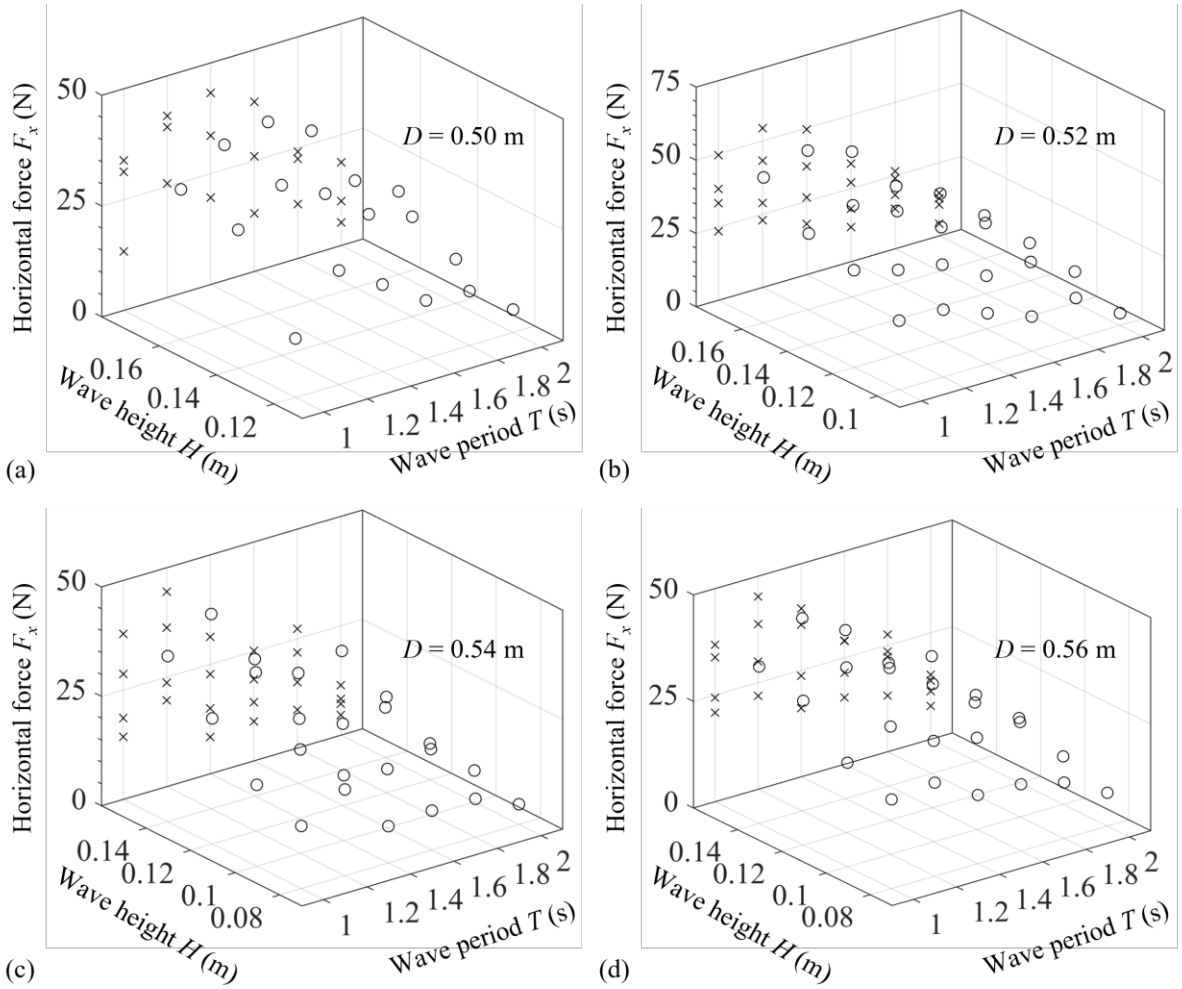

322

323 Fig. 8 Maximum horizontal forces under regular wave impacts for cases with (a) D = 0.50 m;

324 (b) D = 0.52 m; (c) D = 0.54 m; and (d) D = 0.56 m

325

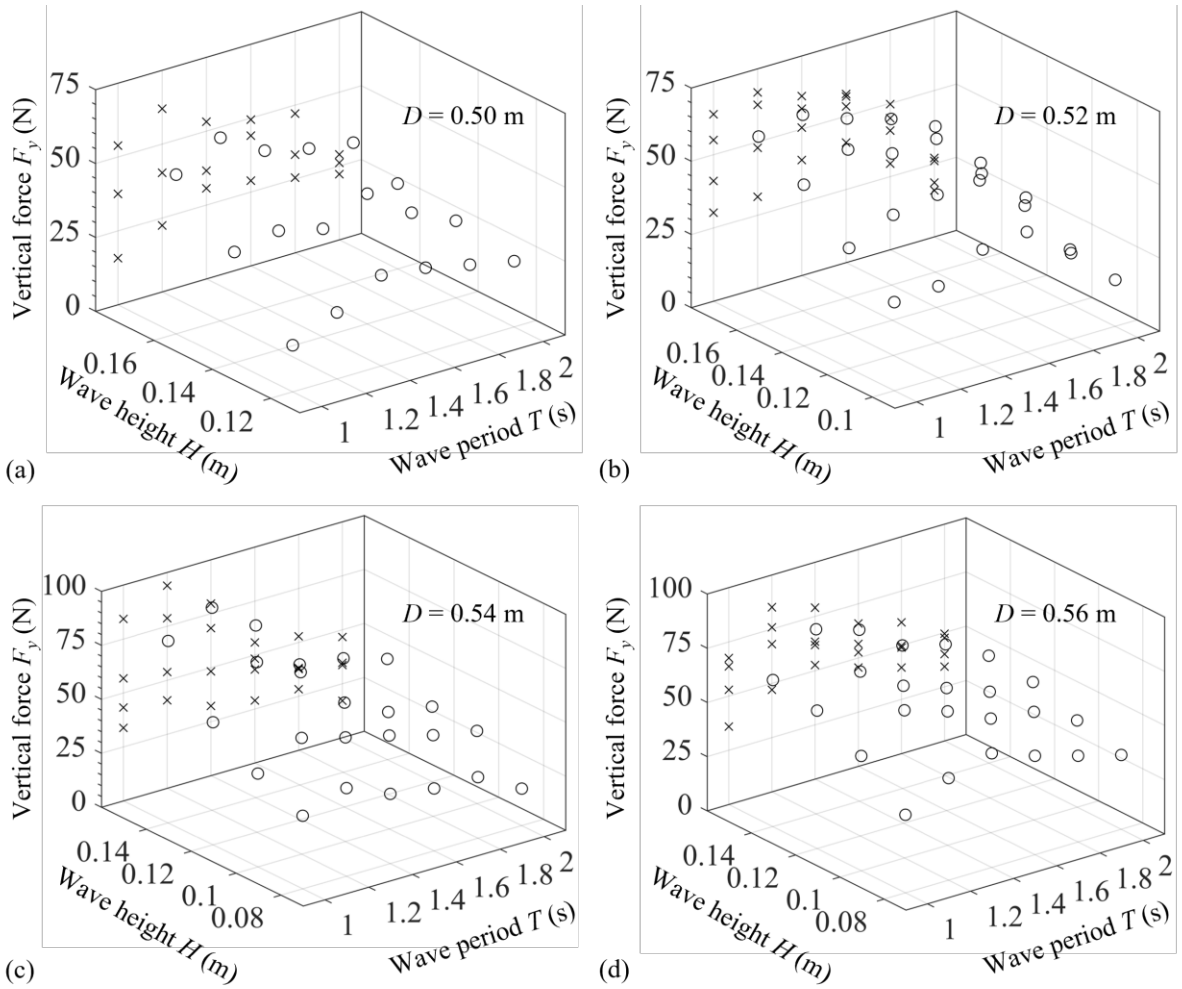

326

327 Fig. 9 Maximum vertical forces under regular wave impacts for cases with (a) D = 0.50 m;

328 (b) D = 0.52 m; (c) D = 0.54 m; and (d) D = 0.56 m

329

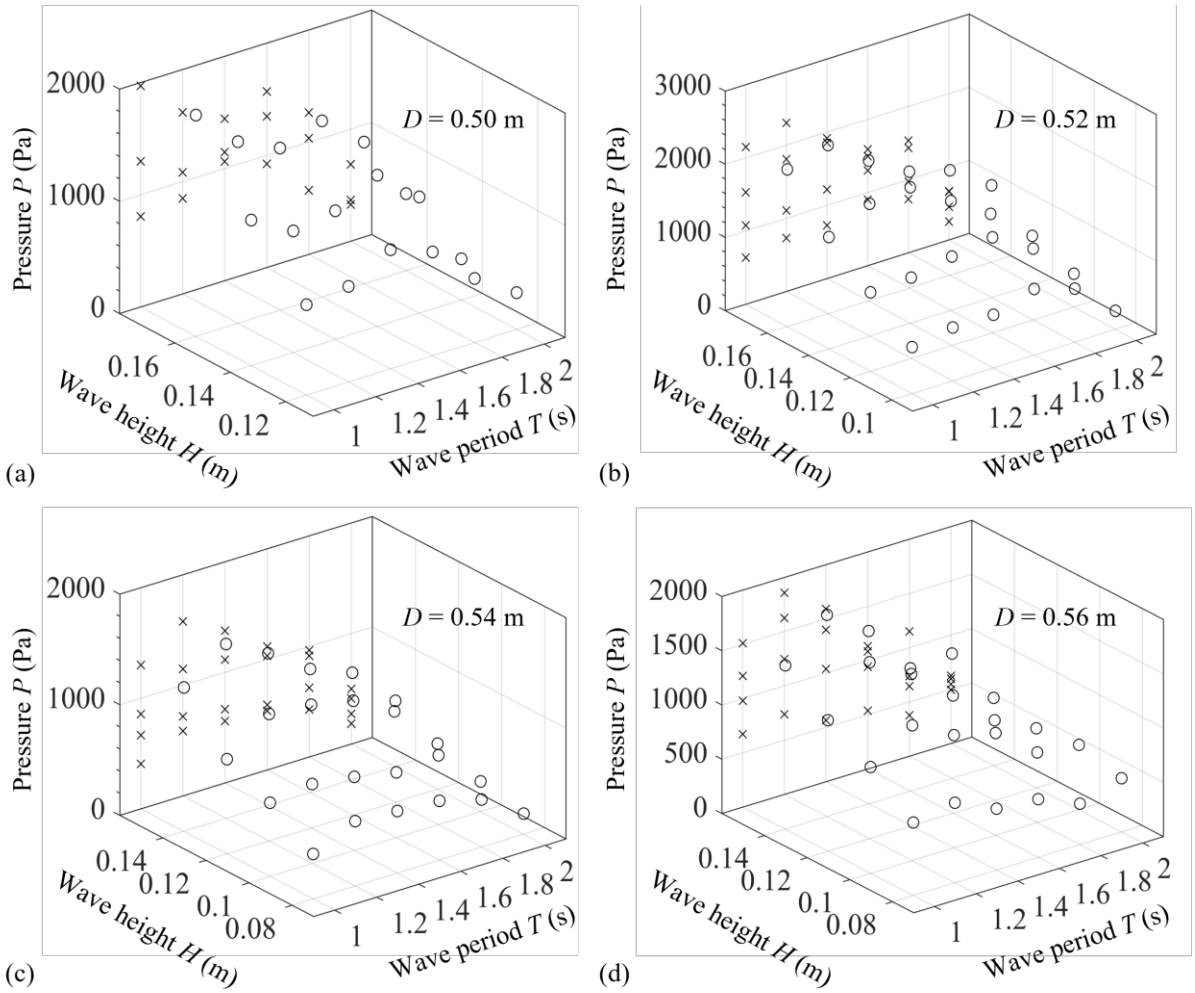

Fig. 10 Maximum pressures under regular wave impacts for cases with (a) D = 0.50 m; (b) D = 0.52 m; (c) D = 0.54 m; and (d) D = 0.56 m

5. ML results

To explore the relationships between wave-induced forces and excitation waves, and to provide a highly efficient tool for stochastic analysis in future studies, this section develops advanced LSTM models for predicting time series wave impacts. The training process, model performance, and tuning of different hyperparameters are presented in this section.

5.1 Development of LSTM models

Advanced deep learning models, which are based on a multi-layer architecture centered on LSTM cells, have been constructed for solitary wave and regular wave impacts, respectively. A total of 294 datasets of the experimental measurements (98 cases, 3 repeated tests for each

case) are utilized for the LSTM training of regular waves, and 90 datasets (30 cases, 3 repeated tests for each case) are used for solitary waves. The changing wave profiles collected from the wave gauges are used as the model input, and the wave force time series are used as the output. During the model training, 70% of the raw data are used as the training set, 15% are used as the test set, and the rest 15% are used as the validations set. A potential benefit of this approach is that the LSTM prediction results can reduce the deviations caused by the repeated tests, since it comprehensively incorporates all the datasets.

To scale up the number of hidden layer neural networks, the accuracy of the operation must first be scrutinized, followed by an analysis of the time demands inherent in sample training and prediction. In an event that the number of neurons contained within the hidden layer is insufficient, the learning accuracy will be reduced and the number of required training iterations will rise commensurately. Conversely, if the number of neurons surpasses a certain threshold, the network's complexity shall escalate, thereby inflating the requisite training time and the number of mandatory weights. It follows that the ultimate output of the neural network hinges on the number of hidden neurons employed. Therefore, in this investigation, a total of 128 hidden neurons are selected after several trials.

Since each node residing within the fully connected layer is connected to all antecedent nodes, its role is to meld the salient characteristics previously distilled from the earlier layer, and then assimilate the hidden patterns intrinsic to the time series at hand. Considering both the computational efficiency and model accuracy, it is found that 64 nodes have been deemed adequate for deployment in the fully connected layer in this context.

Regarded as a critical hyperparameter in both supervised and deep learning, the learning rate governs the capacity of the objective function to converge upon a local minimum within a given timeframe. An optimal learning rate facilitates the objective function's resolution within a reasonable duration of time. In the context of this study, the optimal learning rate has been determined via rigorous experimentation to be 0.005.

The network training is conducted employing TensorFlow, a well-established and documented open-source symbolic math library developed by the Google Brain team for

machine learning applications. This library boasts a flexible data flow architecture, enabling high-performance training of various types of neural networks on multiple platforms, including CPUs, GPUs, and TPUs. The simulations discussed in this paper are carried out on a desktop computer equipped with 12th Intel Core i7-12700K CPUs and an NVIDIA GTX 1080Ti GPU card.

Notably, although a similar structure is used for the two sets of LSTM models for solitary wave and regular wave, their hyperparameters, such as weights and biases, are different due to the differences in their respective input data. Fig. 11 distinctly displays the loss curves of these prediction models during the training process. Fig. 12 presents comparative results of the LSTM prediction wave loads with the experimental measurements. The small loss value after 600 iterations and the good convergence observed from the comparisons prove the good prediction performance of the developed LSTM models.

These experimental-data-based LSTM models have the following advantages as compared with conventional wave loads estimation methods: (a) Fewer deviations because of the raw experimental data used as the training set. Previous ML models usually utilized a few wave parameters (e.g., wave height H and wavelength λ) as the input of the model, while the influence of the changing wave profiles was ignored (Chen et al. 2021; Wang et al. 2021). Also, the deviations in the repetitive tests were often expressed using the mean value and standard deviation, but without being considered in the prediction models. The developed LSTM models overcome this limitation by incorporating the time series datasets obtained from the repeated experiments into the model training. (b) Higher efficiency as compared with numerical simulations. A refined hydrodynamics model usually takes hours or even days to reproduce the wave-bridge interactions and compute the wave loads, which is unacceptable for stochastic analysis involving a large number of calculations. A well-trained LSTM model could predict load characteristics from measured waveforms in seconds. (c) Easier expansions due to its network structures. The design guide specification (AASHTO 2008) also pointed out that one important reason limiting the development of wave load prediction methods is that the measured results are often more applicable to the investigated conditions, while additional

experiments are required for other scenarios. The developed LSTM models could facilitate this approach to a certain extent through transfer learning methods (Weiss et al. 2016), which effectively preserve hidden layers in the network structure, and augment additional layers based on a smaller amount of data.

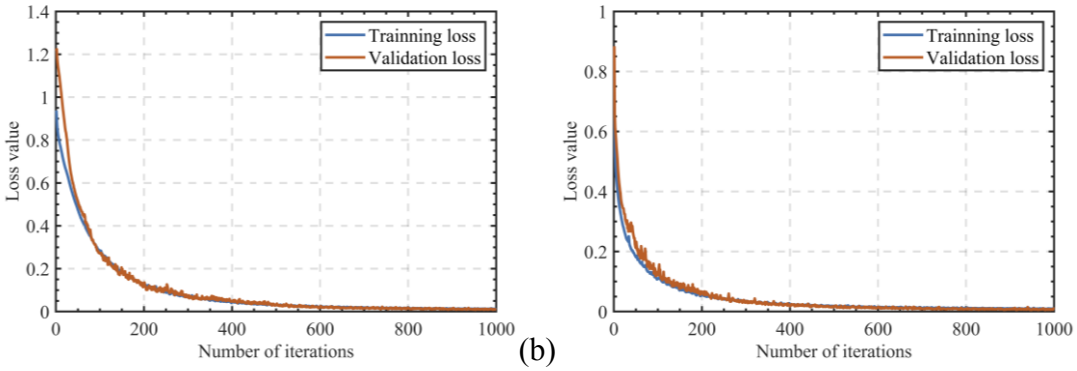

Fig. 11 Loss curves of trained LSTM models in different datasets (a) solitary waves; (b) regular waves

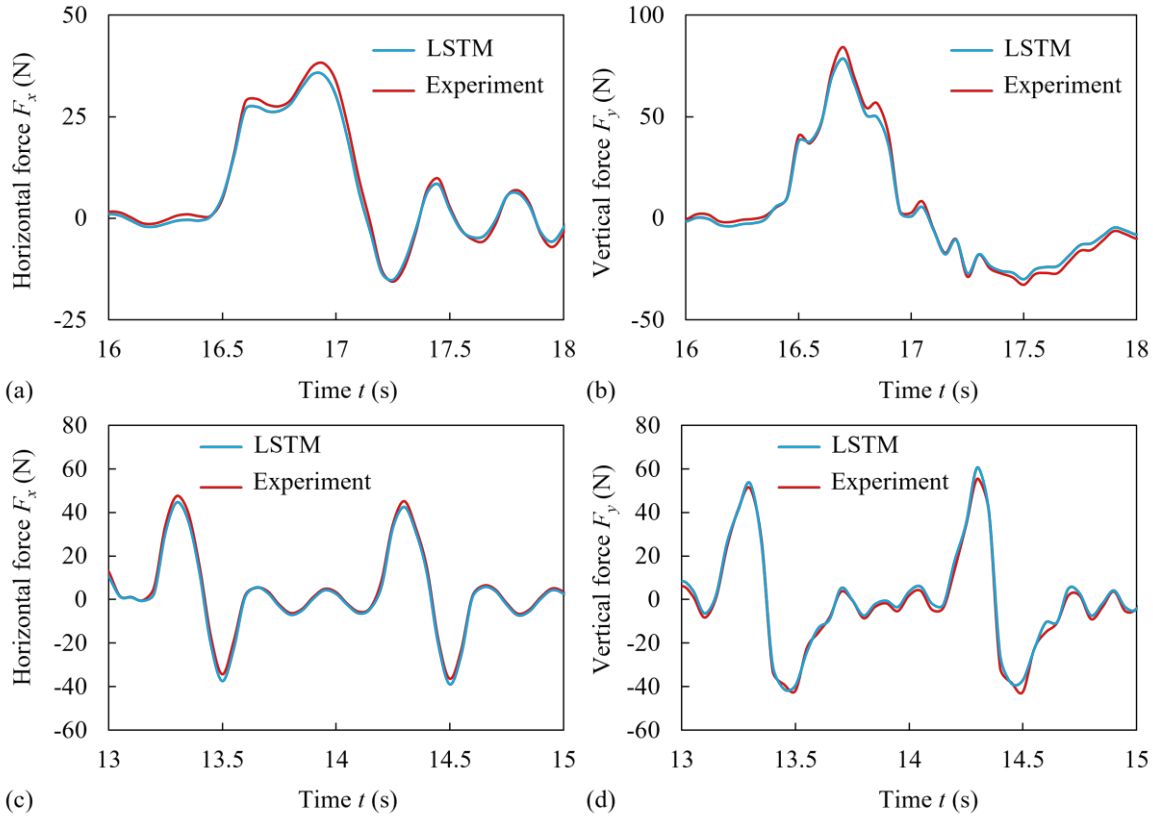

Fig. 12 Comparisons between LSTM predicted results and experimental measurements: (a) F_x of solitary wave case with D = 0.5 m and H = 0.16 m; (b) F_y of solitary wave case with D

409 = 0.5 m and H = 0.16 m; (c) F_y of regular wave case with D = 0.5 m, H = 0.14 m, and T = 1s;
410 and (d) F_y of regular wave case with D = 0.5 m, H = 0.16 m, and T = 1s

411 5.2 Hyperparameter tuning

412 To have a deeper understanding of the developed models, the impacts of hyperparameter
413 configurations on the performance of an LSTM model are explored in this section. Specifically,
414 the effect of learning rate and dropout settings on the model prediction results are discussed.
415 The importance of hyperparameter tuning in optimizing machine learning models is well-
416 recognized. Therefore, comprehending the effect of individual hyperparameters on the model's
417 performance is crucial for customizing the model for a given task. Precisely, determining an
418 appropriate learning rate and dropout rate can significantly enhance the model's predictive
419 capacity. The tested learning rates range from 10^{-4} to 10^{-2}, while the dropout values span from
420 0.2 to 0.7. To assess the influence of hyperparameters on the model prediction results, two
421 performance indicators, mean squared error (MSE) and coefficient of determination (R^2),
422 which were introduced in Section 2, are utilized. These metrics offer a reliable approach for
423 evaluating the model's predictive capability relative to the actual observations.

424 For the solitary wave load LSTM prediction model, Figs. 13 (a) and (b) show the model's
425 predictive performance variation with respect to different learning rates for the same dropout
426 values. Our analysis reveals a quadratic relationship between the model's predictive ability and
427 the learning rate, leading to a single-peak curve in the model performance graph. The optimal
428 learning rate is approximately 0.001. These findings highlight the importance of choosing an
429 appropriate learning rate to optimize the model's prediction capability. On the other hand, Figs.
430 13 (c) and (d) illustrate the change in predictive performance with different dropout values for
431 the same learning rate. Interestingly, no clear trend is observed in the model performance curve,
432 indicating that the impact of dropout on the model's performance is relatively minor. However,
433 it is worth noting that a dropout value of 0.5 typically results in the worst predictive
434 performance, and its use should be avoided in practical applications. Moreover, these analyses
435 reveal that when the learning rate is low (approximately 0.001 to 0.003), the effect of dropout
436 on the model's predictive accuracy is minimal. This finding is significant as it suggests that in

certain scenarios, the dropout value may not be critical to the model's overall performance when the learning rate is sufficiently low.

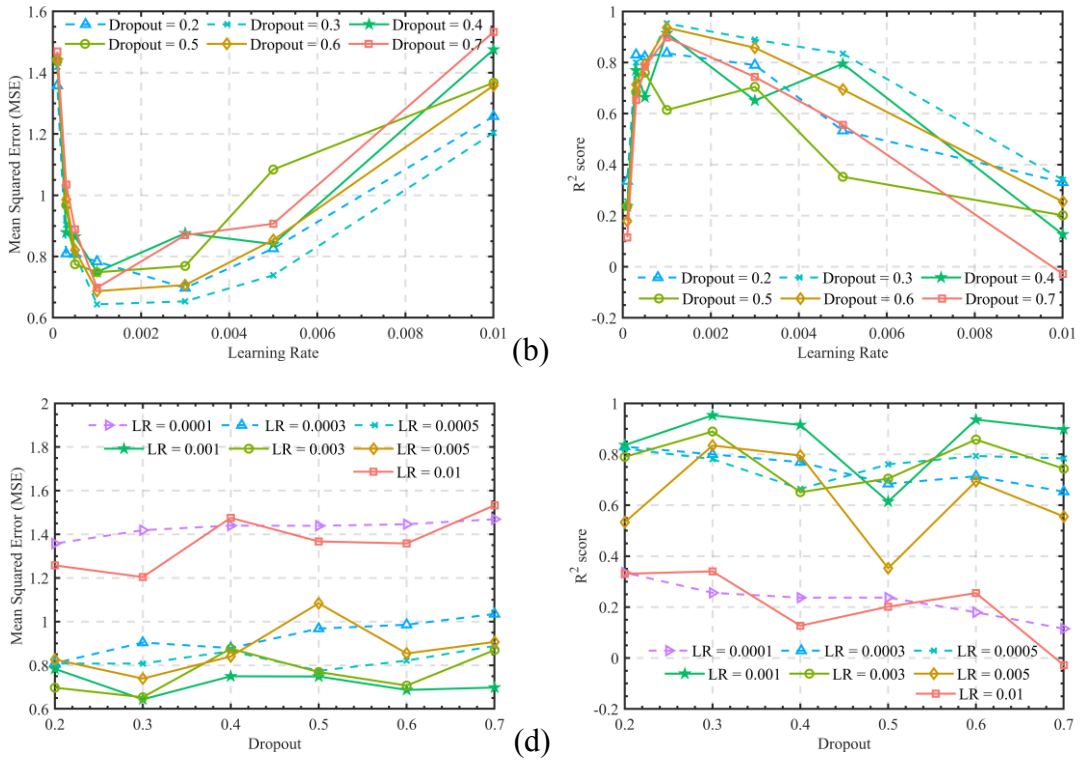

Fig. 13 Hyperparameter tuning results for LSTM prediction model of solitary waves: (a), (b) MSE and R^2 with respect to different learning rates for the same dropout values; and (c), (d) MSE and R^2 with respect to different dropout values for the same learning rate

Tuning results for the LSTM models of regular waves are shown in Fig. 14. Similar to the solitary wave LSTM model, the regular wave model also exhibits an optimal prediction performance when the learning rate is set to 0.001, and the changes in the predictive efficacy with respect to the variation of dropout values are not significant. It is worth noting that both models demonstrate the same optimal hyperparameter configuration, where the learning rate is set to 0.001, and the dropout rate is set to 0.3. This observation highlights the importance of fine-tuning hyperparameters for machine learning models, as finding the optimal combination of hyperparameters can significantly improve the model's performance. Furthermore, the consistent hyperparameter configuration for the two models suggests that these settings could

be a good starting point for developing similar models in the future, particularly for predicting loads induced by ocean waves.

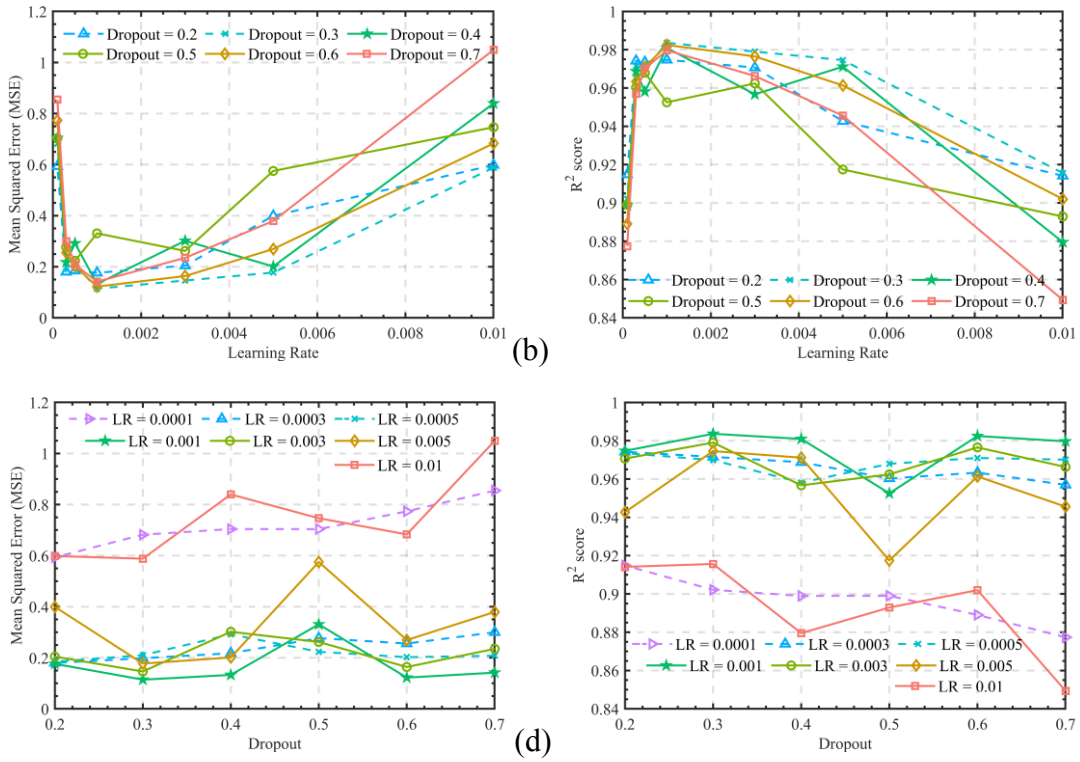

Fig. 14 Hyperparameter tuning results for LSTM prediction model of regular waves: (a), (b) MSE and R^2 with respect to different learning rates for the same dropout values; and (c), (d) MSE and R^2 with respect to different dropout values for the same learning rate

6. Conclusions

This paper presents a hydrodynamic experiment on wave-bridge interactions and the development of data-driven LSTM techniques for time series forecasting of wave forces. Specifically, a 1:30 scale bridge superstructure specimen is used for the wave test in the wave channel under different solitary wave and regular wave conditions. Time histories of wave profiles, wave-induced forces, and pressures are measured and served as a dataset basis for the training of LSTM models. High-performance LSTM prediction models are developed through the tuning of different hyperparameters. From the measurements of the experimental data and the establishment of LSTM models, the following conclusions can be made:

1. Through experimental measurements of wave-induced pressure on the bridge span, it is observed that there is a concentrated uplift pressure on the seaward side (facing the

waves) of the deck under all the solitary wave conditions and most regular wave conditions. The maximum value of the pressure P at the seaward side could be 20 – 30% larger than the opposite side and could reach 2304.54 Pa. This phenomenon may induce a large overturning moment on the deck, affecting structural stability.

2. After comparing the measured wave forces under different wave conditions, it is found that under similar wave amplitudes and clearances, solitary waves and regular waves may cause close vertical forces on the deck, while the horizontal forces caused by regular waves are much larger. This means the different wave profiles may also affect the wave forces and should be accounted for in the prediction methods.
3. LSTM models with 128 hidden neurons, 64 nodes in each connected layer, and a learning rate of 0.001 are developed to have the optimal forecasting performance for wave-induced forces. Through the investigations on different hyperparameters, it is found that when the learning rate is low (from 0.001 to 0.003), the effect of dropout on the model's predictive accuracy is relatively small.
4. The experimental-data-based LSTM prediction models have the advantages of less deviation and higher efficiency. LSTM models for both wave types have satisfying R^2-source values close to 0.98, and small MSEs at a 10^{-1} level. The well-trained model could predict the wave force time series based on the excitation wave profiles in seconds.

Acknowledgments

The study has been supported by the Research Grants Council of Hong Kong (PolyU 15225722 and PolyU 15221521) and department of Civil and Environmental Engineering of the Hong Kong Polytechnic University (1-WZ0B). The support is gratefully acknowledged. The opinions and conclusions presented in this paper are those of the authors and do not necessarily reflect the views of the sponsoring organizations.

References

AASHTO. (2008). *Guide specifications for bridges vulnerable to coastal storms*. American

500 Association of State Highway and Transportation Officials, Washington, US.
501 Ataei, N., and Padgett, J. E. (2013). Probabilistic modeling of bridge deck unseating during
502 hurricane events. *Journal of Bridge Engineering*, *18*(4), 275–286.
503 Azadbakht, M., and Yim, S. C. (2016). Effect of trapped air on wave forces on coastal bridge
504 superstructures. *Journal of Ocean Engineering and Marine Energy*, *2*(2), 139–158.
505 Bradner, C., Schumacher, T., Cox, D., and Higgins, C. (2011). Experimental setup for a large-
506 scale bridge superstructure model subjected to waves. *Journal of Waterway, Port, Coastal*
507 *and Ocean Engineering*, *137*(1), 3–11.
508 Cai, Y., Agrawal, A., Qu, K., and Tang, H. S. (2018). Numerical Investigation of Connection
509 Forces of a Coastal Bridge Deck Impacted by Solitary Waves. *Journal of Bridge*
510 *Engineering*, *23*(1), 04017108.
511 Chen, X., Chen, Z., Xu, G., Zhuo, X., and Deng, Q. (2021). Review of wave forces on bridge
512 decks with experimental and numerical methods. *Advances in Bridge Engineering*, *2*(1),
513 1–24.
514 Chorzepa, M. G., Saeidpour, A., Christian, J. K., and Durham, S. A. (2016). Hurricane
515 vulnerability of coastal bridges using multiple environmental parameters. *International*
516 *Journal of Safety and Security Engineering*, *6*(1), 10–18.
517 Cuomo, G., Shimosako, K. ichiro, and Takahashi, S. (2009). Wave-in-deck loads on coastal
518 bridges and the role of air. *Coastal Engineering*, *56*(8), 793–809.
519 Ding, Y., Ma, R., Shi, Y. D., and Li, Z. X. (2018). Underwater shaking table tests on bridge
520 pier under combined earthquake and wave-current action. *Marine Structures*, *58*, 301–
521 320.
522 Dong, Y., and Frangopol, D. M. (2016). Probabilistic Time-Dependent Multihazard Life-Cycle
523 Assessment and Resilience of Bridges Considering Climate Change. *Journal of*
524 *Performance of Constructed Facilities*, *30*(5).
525 Guo, A., Liu, J., Chen, W., Bai, X., Liu, G., Liu, T., Chen, S., and Li, H. (2016). Experimental
526 study on the dynamic responses of a freestanding bridge tower subjected to coupled
527 actions of wind and wave loads. *Journal of Wind Engineering and Industrial*

528 *Aerodynamics*, *159*(10), 36–47.
529 Hecht-Nielsen, R. (1992). Theory of the backpropagation neural network. *Neural networks for*
530 *perception*, 65–93.
531 Hochreiter, S. (1998). The vanishing gradient problem during learning recurrent neural nets
532 and problem solutions. *International Journal of Uncertainty, Fuzziness and Knowlege-*
533 *Based Systems*, *6*(2), 107–116.
534 Istrati, D., and Buckle, I. (2019). Role of trapped air on the tsunami-induced transient loads
535 and response of coastal bridges. *Geosciences (Switzerland)*, *9*(4).
536 Jia, L., Zhang, Y., Zhu, D., and Dong, Y. (2022). 3D Numerical Modeling and Quantification
537 of Oblique Wave Forces on Coastal Bridge Superstructures. *Journal of Marine Science*
538 *and Engineering*, *10*(7), 860.
539 Jin, J., and Meng, B. (2011). Computation of wave loads on the superstructures of coastal
540 highway bridges. *Ocean Engineering*, *38*(17–18), 2185–2200.
541 Meng, B., and Jin, J. (2007). Uplift wave load on the superstructure of coastal bridges. *New*
542 *Horizons and Better Practices*, 1-10.
543 Moideen, R., and Behera, M. R. (2021). Numerical investigation of extreme wave impact on
544 coastal bridge deck using focused waves. *Ocean Engineering*, *234*, 109227.
545 Padgett, J., Desroches, R., Nielson, B., Yashinsky, M., Kwon, O. S., Burdette, N., and Tavera,
546 E. (2008). Bridge damage and repair costs from Hurricane Katrina. *Journal of Bridge*
547 *Engineering*, *13*(1), 6–14.
548 Qu, K., Tang, H. S., Agrawal, A., Cai, Y., and Jiang, C. B. (2018). Numerical investigation of
549 hydrodynamic load on bridge deck under joint action of solitary wave and current. *Applied*
550 *Ocean Research*, *75*, 100–116.
551 Robertson, I. N., Riggs, R. H., Yim, S. C. S., and Young, Y. L. (2007). Lessons from Hurricane
552 Katrina storm surge on bridges and buildings. *Journal of Waterway, Port, Coastal and*
553 *Ocean Engineering*, *133*(6), 463–483.
554 Robertson, I. N., Yim, S., and Tran, T. (2011). Case study of concrete bridge subjected to
555 hurricane storm surge and wave action. *Solutions to Coastal Disasters 2011 - Proceedings*

556 *of the 2011 Solutions to Coastal Disasters Conference*, 728–739.
557 Seiffert, B., Hayatdavoodi, M., and Ertekin, R. C. (2014). Experiments and computations of
558 solitary-wave forces on a coastal-bridge deck. Part I: Flat plate. *Coastal Engineering*, *88*,
559 194–209.
560 Seiffert, B. R. (2014). *Tsunami and Storm Wave Impacts on Coastal Bridges*. PhD thesis,
561 University of Hawai'i at Manoa, US.
562 Seiffert, B. R., Cengiz Ertekin, R., and Robertson, I. N. (2016). Effect of Entrapped Air on
563 Solitary Wave Forces on a Coastal Bridge Deck with Girders. *Journal of Bridge*
564 *Engineering*, *21*(2), 4015036.
565 Seiffert, B. R., Ertekin, R. C., and Robertson, I. N. (2015). Wave loads on a coastal bridge deck
566 and the role of entrapped air. *Applied Ocean Research*, *53*, 91–106.
567 Sherstinsky, A. (2020). Fundamentals of Recurrent Neural Network (RNN) and Long Short-
568 Term Memory (LSTM) network. *Physica D: Nonlinear Phenomena*, *404*, 132306.
569 Wang, J., Xue, S., and Xu, G. (2021). A hybrid surrogate model for the prediction of solitary
570 wave forces on the coastal bridge decks. *Infrastructures*, *6*(12), 170.
571 Weiss, K., Khoshgoftaar, T. M., and Wang, D. D. (2016). A survey of transfer learning. *Journal*
572 *of Big Data*, *3*(1), 1–40.
573 Xiang, T., and Istrati, D. (2021). Assessment of extreme wave impact on coastal decks with
574 different geometries via the arbitrary lagrangian-eulerian method. *Journal of Marine*
575 *Science and Engineering*, *9*(12), 1342.
576 Xiao, H., and Huang, W. (2008). Numerical modeling of wave runup and forces on an idealized
577 beachfront house. *Ocean Engineering*, *35*(1), 106–116.
578 Xu, G., Wei, H., Xue, S., Wang, J., and Li, Y. (2022). Predicting wave forces on coastal bridges
579 using genetic algorithm enhanced ensemble learning framework. *Ocean Engineering*, *266*,
580 112963.
581 Xu, Y., Øiseth, O., and Moan, T. (2018). Time domain simulations of wind- and wave-induced
582 load effects on a three-span suspension bridge with two floating pylons. *Marine Structures*,
583 *58*, 434–452.

584 Yuan, P., Zhu, D., and Dong, Y. (2021). Spatial failure mechanism of coastal bridges under
585 extreme waves using high-efficient pseudo-fluid-structure interaction solution scheme.
586 *Ocean Engineering*, *240*, 109894.
587 Zhang, J., Zhu, B., Kang, A., Yin, R., Li, X., and Huang, B. (2020). Experimental and
588 numerical investigation of wave-current forces on coastal bridge superstructures with box
589 girders. *Advances in Structural Engineering*, *23*(7), 1438–1453.
590 Zhang, W., Li, H., Li, Y., Liu, H., Chen, Y., and Ding, X. (2021). Application of deep learning
591 algorithms in geotechnical engineering: a short critical review. *Artificial Intelligence*
592 *Review*, *54*(8), 5633–5673.
593 Zhu, D., and Dong, Y. (2020). Experimental and 3D numerical investigation of solitary wave
594 forces on coastal bridges. *Ocean Engineering*, *209*, 107499.
595 Zhu, D., Dong, Y., and Frangopol, D. M. (2022). Experimental and numerical investigation on
596 wave impacts on box-girder bridges. *Structure and Infrastructure Engineering*, *18*(10–
597 11), 1379–1397.
598 Zhu, D., Li, Y., and Dong, Y. (2021). Reliability-based retrofit assessment of coastal bridges
599 subjected to wave forces using 3D CFD simulation and metamodeling. *Civil Engineering*
600 *and Environmental Systems*, *38*(1), 59–83.
601 Zhu, D., Yuan, P., and Dong, Y. (2021). Probabilistic performance of coastal bridges under
602 hurricane waves using experimental and 3D numerical investigations. *Engineering*
603 *Structures*, *242*, 112493.
604